Character of Convective Systems Producing Short-Term Heavy Precipitation in Central China Revealed by Kilometer and Minute Interval Observations

Zitong CHEN[1], Yunying LI[1,2*], Zhiwei ZHANG[1,3], Jing SUN[1,4], Chengzhi YE[5], and Anyuan XIONG[6]

1 *College of Meteorology and Oceanography, National University of Defense Technology, Changsha* 410073
2 *High Impact Weather Key Laboratory of China Meteorological Administration, Changsha* 410073
3 *Unit No.* 92192 *of Chinese People's Liberation Army, Ningbo* 315000
4 *Hubei Key Research Laboratory for Heavy Rain Monitoring and Warning, Institute of Heavy Rain, China Meteorological Administration, Wuhan* 430223
5 *Institute of Meteorological Sciences of Hunan Province, Hunan Meteorological Bureau, Changsha* 410118
6 *National Meteorological Information Centre, China Meteorological Administration, Beijing* 100081

(Received 31 August 2023; in final form 10 February 2024)

ABSTRACT

Accurate forecasting of heavy precipitation in central China is still a challenge, within which a key issue is our still incomplete understanding of the convective systems (CSs) responsible for such events. In this study, through use of an iterative rain-cell tracking algorithm, the macroscale characteristics (scale, intensity, duration, etc.) of the CSs that produced 595 short-term heavy precipitation events in Hunan Province, central China, are quantitatively analyzed, based on radar reflectivity, echo top, and rainfall observations at 1-km and 6-min intervals in April–September of 2016–2018. The results show that CSs present significant seasonal and diurnal features. Spring CSs usually cover a larger echo area with stronger convective cores and thus generate more precipitation than summer CSs, though summer CSs develop more vigorously and frequently. CSs initiated at 1400–1600 local time are characterized by the strongest convection and a smaller spatiotemporal scale, causing violent and transient showers with typical areal precipitation of 0.5–1 mm km^{-2}, but less total precipitation. Further analyses of the relationships among the scale, intensity, duration, and total precipitation of CSs reveal that the convective intensity is linearly correlated to the spatiotemporal scale of CSs, with the duration increasing on average by 0.0372 h dBZ^{-1}; the echo area is significantly correlated to the total precipitation, and the duration and rainfall amount are connected with the area expansion rate (AER) of CSs: when the AER exceeds 50%, CSs expand rapidly with increasing total precipitation, but the duration is shorter. These findings provide a helpful reference for the forecasting of short-term heavy precipitation induced by CSs in central China.

Key words: convective system, radar reflectivity factor, total precipitation, iterative rain-cell tracking

Citation: Chen, Z. T., Y. Y. Li, Z. W. Zhang, et al., 2024: Character of convective systems producing short-term heavy precipitation in central China revealed by kilometer and minute interval observations. *J. Meteor. Res.*, **38**(3), 530–541, doi: 10.1007/s13351-024-3150-x.

1. Introduction

Convective systems (CSs) are meso–micro-scale weather systems generated by violent vertical ascending motion of the near-surface atmosphere. CSs generally last for several to tens of hours, with horizontal scales ranging from dozens to hundreds of kilometers (Tian et al., 2015; Schroeer et al., 2018). They are often accompanied by severe convective weather, such as short-term heavy precipitation, thunderstorm gales, tornadoes, and/or hail (Liu et al., 2014; Ma et al., 2021), causing severe damage to people's lives and property, and even huge social impacts (Meng et al., 2013; Rasmussen et al., 2016; Houze, 2018).

Hunan Province (24.6°–30.2°N, 108.7°–114.3°E), located in central China, is a region prone to frequent and disastrous short-term heavy precipitation associated with CSs in spring and summer (Zheng et al., 2013; Tian et

Supported by the Hunan Provincial Natural Science Foundation of China (2021JC0009) and National Natural Science Foundation of China (U2242201 and 42075077).

*Corresponding author: ghlyy@mail.iap.ac.cn

al., 2015). Studies have been carried out to gain some understanding of the short-term heavy rainfall events in this region, and have found that rainstorms usually have a high echo top but low storm centroid elevation (Lan et al., 2022), occurring in summer more than in spring (Yao et al., 2020). However, systematic and quantitative statistical analyses of CSs related to short-term heavy precipitation in Hunan Province remain lacking, which warrants further investigation into the common characteristics of the convective processes in this region.

The relationships between CS macroscale characteristics (such as scale, intensity, and duration) and short-term heavy precipitation have been analyzed in previous studies based on satellite and radar data (Chen et al., 2020; Fu et al., 2020; Chen et al., 2021). For example, CSs moving out of the Tibetan Plateau appear with larger cloud areas and stronger intensities than those staying within the plateau, making smaller contributions to local total precipitation but leading to 10%–20% of all heavy precipitation events in the Sichuan basin (Hu et al., 2016; Mai et al., 2021; Zhang et al., 2021). Li et al. (2021) found that mesoscale convective systems (MCSs) in South China usually develop faster and have a shorter lifetime, which bring more intense precipitation than other systems. So far, the quantitative relationship between CS macroscale characteristics and precipitation in central China has not been specifically analyzed, yet such a quantitative correlation is essential for estimating the potential precipitation amount and providing early warning of disasters (Marra et al., 2016; Cristiano et al., 2017). It also helps to extend the predictability of certain weather events and is conducive to understanding the nonlinear processes during the lifetime of a CS (Goudenhoofdt and Delobbe, 2013; Hou and Wang, 2017). The present work aims to explore the quantitative relationship in Hunan Province of central China based on local radar observations, which have considerable advantages in studying local CSs given the high spatiotemporal resolution of such radar products (Chen et al., 2012; Utsav et al., 2017; Samanta et al., 2021).

Tracking CSs and recording their spatiotemporal information are critical steps toward exploring the features of CSs (Lakshmanan and Smith, 2010). Several tracking algorithms have been developed and subsequently improved. For example, the correlation tracking algorithm is relatively simple and efficient, but with a formidable computational load amount (Carvalho and Jones, 2001). The area-overlapping algorithm requires the overlapping area of CSs at two adjacent moments, and struggles to track CSs with a small area or fast-moving speed (Haberlie and Ashley, 2018; Chen et al., 2019; Zhang et al., 2022). Accordingly, a new iterative rain-cell tracking (IRT) algorithm was proposed by Moseley et al. (2013, 2019), which offers a better solution to the tracking of small-area or fast-moving CSs by considering both the atmospheric advection and the overlapping area, and thus has been widely applied (Nissen and Haerter, 2021; Meredith et al., 2023). Thus, we chose the IRT algorithm in this work to track CSs in Hunan Province of China.

The remainder of this paper is organized as follows: Section 2 introduces the data, tracking method, and the CS parameters. Sections 3 and 4 present the statistical characteristics of CSs and their correlations with precipitation, respectively. Finally, a summary and discussion are provided in Section 5.

2. Data and methods

2.1 *Data*

A minute-scale benchmark dataset of quantitative precipitation estimation and forecasting (QpefBD) is employed in this work, containing radar products and precipitation data of 622 short-term heavy precipitation events in Hunan Province from April to September 2016–2018 (Xiong et al., 2022). A short-term heavy precipitation event starts when the hourly precipitation becomes equal to or greater than 20 mm and ends when the criterion is subsequently not satisfied (Tian et al., 2015; Xiong et al., 2022). For each event, the S-band weather radar station closest to the event's location is selected to avoid repeated observation by multiple radars. The precipitation data in QpefBD are gridded data collected from national automatic weather stations, and radar products contain echo top and radar reflectivity factor data at altitudinal levels from 2 to 5 km on the constant altitude plan position indicator (CAPPI). They all center on the radar station with a 0.01° × 0.01° spatial resolution and 6-min temporal resolution. The locations of radar stations in Hunan Province are shown in Fig. 1a, and the numbers of events recorded by each radar station are in Fig. 1b.

2.2 *Tracking algorithm and quality control*

In most regions, CSs usually have a spatial extent of more than 10 km and a reflectivity factor greater than 25 dBZ (Berg et al., 2013; Shehu and Haberlandt, 2022). Most develop at approximately 3 km above sea level and can be detected by radars (Peter et al., 2015; Sun et al., 2019). In this paper, CSs are defined by a continuous area larger than 100 km^2 of reflectivity over 25 dBZ, using the CAPPI reflectivity factor data at an altitude of 3 km.

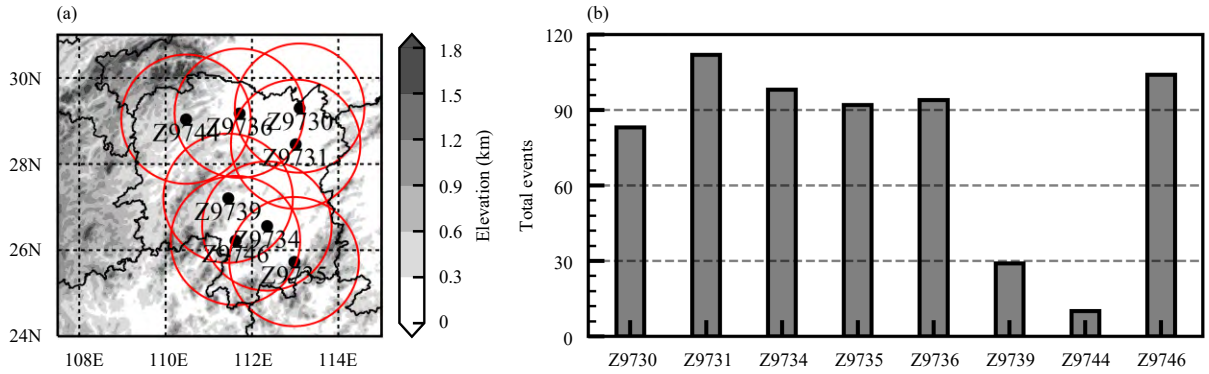

Fig. 1. (a) Locations of the radar stations (black dots) and their detection ranges (red circles) in Hunan Province, with the grayscale shading showing the terrain elevation (km). (b) Numbers of short-term heavy precipitation events at each radar station in (a).

The procedure of the IRT algorithm is illustrated in Fig. 2. CSs are identified and their echo area, intensity, and center of mass are recorded at each timestep. CSs at two consecutive moments will be marked as the same target if they are found to be area-overlapped, building up the preliminary tracks. After iteratively calculating the advection field from the tracks, all CSs at timestep t are advected by the advection field and checked for overlaps with non-advected CSs at timestep $t + 1$. Tracks with abnormal echo area variations are terminated when merging or splitting occurs. If a small CS combines with a much larger one, the larger one continues to be tracked since the merged CSs might not be distinct from the larger of the two. Otherwise, all involved tracks are terminated in a merging/splitting incident, which could reduce the impact of merging/splitting on the area expansion as much as possible. Detailed information of the IRT algorithm can be found in Moseley et al. (2013, 2019). Once all tracks have been obtained, spatiotemporal matching between the track information and surface precipitation data is performed, requiring that only precipitation within CS ranges is considered to have been produced by the CSs.

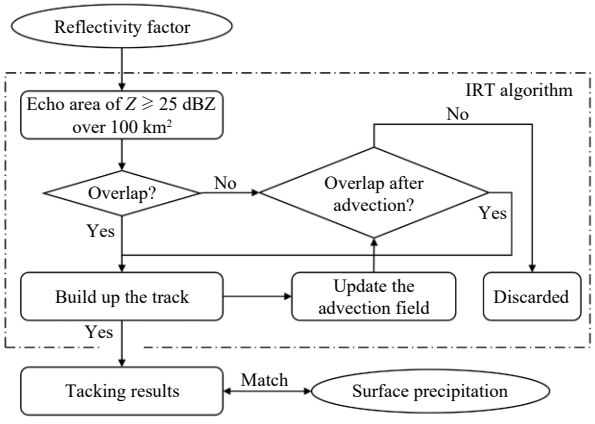

Fig. 2. Flowchart of the IRT algorithm used to identify the CSs in this work.

Quality control of the CSs observed by radars is carried out as follows. CSs with a duration shorter than 1 h are excluded since such CSs account for only 10% of all CSs, with most lasting for 1–3 h. It also needs to be determined whether CSs were only observed for a part of their lifetime, since the radar data are collected from individual radar stations. Here, we use two similar relative occurrence times to select those CSs experiencing different stages during their lifetime. Relative occurrence times of the maximum convective intensity and the maximum size are used to divide the lifetime into development, maturation, and dissipation stages for typical MCSs (Futyan and del Genio, 2007; Chen et al., 2020). Occurrence times of the maximum reflectivity factor (Z) and the maximum echo area are labeled by T_Z and T_a, respectively, and their relative occurrence times can be represented by r_Z and r_a:

$$r_z = \frac{T_Z}{d}, \tag{1}$$

$$r_a = \frac{T_a}{d}, \tag{2}$$

where d is the rain duration. Relatively loose restrictions of $r_Z \geqslant 0.1$ and $r_a \leqslant 0.8$ are used in this work after several trials. Ultimately, 595 CS events are obtained and used for further analysis.

2.3 *CS parameters*

Parameters used in this work represent the spatiotemporal scale, convective intensity, and precipitation of CSs (Table 1). The echo area refers to the area with Z equal to or larger than 25 dBZ, while the area expansion rate (AER) refers to the change in echo area between timesteps t and $t + 1$ divided by the echo area at timestep t, with S_t and S_{t+1} representing the echo area at timesteps

Table 1. CS parameters used in this study

Parameter	Description
d (h)	Duration
Z_{max}/Z_{mean} (dBZ)	Maximum/mean reflectivity factor (Z) of a CS
Echo area (km^2)	Echo area with $Z \geqslant 25$ dBZ
AER (%)	Echo area expansion per unit timestep
Echo top (km)	Highest altitude of $Z \geqslant 18$ dBZ
Convective fraction	Echo area of $Z \geqslant 40$ dBZ divided by the echo area
Total precipitation (mm)	Total spatiotemporal surface precipitation from a CS
Areal precipitation (mm km^{-2})	6-min surface precipitation per unit echo area within the CS range
Precipitation duration ratio	Precipitation duration divided by CS duration
HPAR	Number of heavy precipitation (over 2.5 mm in 6 min) pixels divided by the number of precipitation pixels.

t and $t + 1$, respectively (Chen et al., 2020):

$$\mathrm{AER} = \frac{S_{t+1} - S_t}{S_t}. \tag{3}$$

A value of 40 dBZ is typically used to identify the core of a convective storm (Houze et al., 2015; Shehu and Haberlandt, 2022). Here, the convective fraction is calculated as the echo area of Z equal to or larger than 40 dBZ divided by the whole echo area, characterizing the relative size of strong convective regions in the clouds (Rasmussen et al., 2016).

Total precipitation, areal precipitation, and the heavy precipitation area ratio (HPAR) provide the macroscale characteristics of CS precipitation. Total precipitation is defined as the total spatiotemporal surface precipitation generated by a CS, while areal precipitation refers to the 6-min cumulative precipitation per unit echo area. The above two parameters reflect the ability of CSs to produce heavy precipitation. The grid points with precipitation exceeding 2.5 mm in 6 min, which is the top 5% of precipitation intensity, are labeled as heavy precipitation pixels, so the HPAR represents the proportion of heavy precipitation pixels with respect to all precipitation pixels.

3. Macroscale characteristics of CSs

3.1 *Stronger intensity but less total precipitation in summer*

The scale and intensity of CSs in summer (June–August) differ from those in spring (April–May). CSs in summer and spring last on average for 2.4 and 2.2 h, respectively, with maximum echo areas of 1800 and 2900 km^2 (Figs. 3a, b). Summer CSs have a longer duration and smaller size, especially those in June, which on average last for 2.6 h. The AER does not show obvious seasonal differences, being more than 60% on average (Fig. 3c). Compared with spring CSs, summer CSs develop powerfully and with stronger average intensity, a higher echo top, and higher convective fraction; the mean intensity is 35.6 dBZ and the echo top even exceeds 16 km (Figs. 3d–f). However, overall, spring CSs have a higher maximum intensity than summer CSs, at 52.1 dBZ compared to 50.6 dBZ (Fig. 3g). The proportion of spring CSs with severe intensity is slightly higher, showing more convective efficiency in spring (Fig. 3h). Each spring CS produces a surface precipitation amount of approximately 33,800 mm, while in summer this figure is 28,200 mm on average, though spring CSs occur less than summer ones (Fig. 3i). Therefore, spring CSs are characterized by more intensive convection and more total precipitation, along with a lower frequency of short-term heavy precipitation events. This is similar to the results in Feng et al. (2019), which demonstrated that spring MCSs feature deeper convection with a larger stratiform rain area and higher volume of rainfall compared with summer MCSs in the east of the US Rocky Mountains.

Precipitation characteristics correspond to the scale and intensity of CSs. Summer CSs produce precipitation across almost their entire lifetime, as the precipitation duration ratio is more concentrated from 0.95 to 1 compared with spring CSs (Figs. 4a, b). Heavy precipitation occurs in more regions of summer CSs, which corresponds to stronger mean convection (Figs. 4c, d and 3d–f). However, summer CSs not only extend less spatially (Fig. 3b), but their maximum precipitation intensity is also slightly weaker than spring CSs, meaning that local heavier precipitation exists in spring CSs (Figs. 4e, f). In other words, spring CSs can produce higher total precipitation and heavier local precipitation, even though the atmospheric conditions in summer are more favorable for generating CSs. With higher average temperature in summer, precipitation particles are more easily evaporated, and their values of median volume diameter are found to be the least (highest) in summer (spring) (Lavanya et al., 2019), leading to the lower total precipitation of summer CSs.

In summary, summer CSs tend to develop more vigorously than spring CSs and with greater convective fraction, a higher echo top, and stronger mean convection,

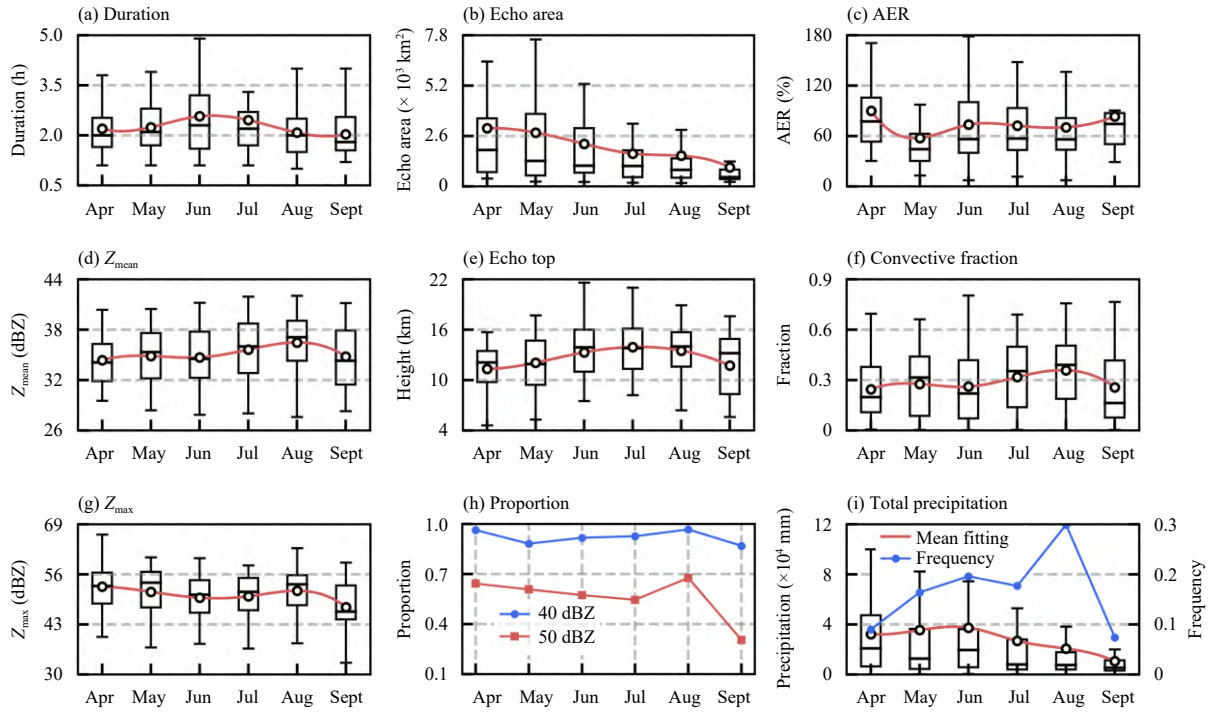

Fig. 3. Distributions of CS parameters from April to September: (a) duration (h), (b) maximum echo area (10^3 km^2), (c) maximum AER (%), (d) Z_{mean} (dBZ), (e) maximum echo top (km), (f) maximum convective fraction, (g) Z_{max} (dBZ), (h) proportion of CSs with Z_{max} over 40 (blue line) and 50 dBZ (red line), (i) total precipitation of each CS (box plot, 10^4 mm) and event frequency (blue line). Black circles in boxplots represent the mean values, with black horizontal lines representing the medians. Red curves in boxplots represent the spline interpolation curve of the mean values.

contributing to the longer duration and higher HPAR of summer CSs (Fig. 5). However, spring CSs cover larger horizontal ranges and contain stronger convective cores, which determine the maximum precipitation intensity. A wider echo area and active convective core are the characteristics most responsible for spring CSs generating heavier total precipitation.

3.2 *Smaller scale but violent showers in the afternoon*

CSs are influenced by the diurnal cycle of solar radiation and atmospheric thermodynamics, leading to the diurnal evolution of short-term heavy precipitation (Chen et al., 2018; Gao et al., 2019). The initiation of a CS can be represented by the first moment of its track. CSs initiate diurnally in a bimodal structure peaking at 1300 and 1600 local time (LT = UTC + 8; Fig. 6a), showing differences with CSs that peak in the afternoon and early morning in the Yangtze–Huai River basin (He et al., 2017) and South China (Li et al., 2021). Most CSs in Hunan Province occur more frequently in the daytime than at night, though they tend to last for a shorter time in the day, especially at the two peak moments when their duration tends to be around 2 h (Fig. 6a). Similarly, short-term heavy precipitation mostly happens in the afternoon (Fig. 7).

CSs during the peak initiation period of 1400–1600 LT lead to significant convective precipitation. They are equipped with the strongest convection cores (Figs. 6b, c) but a smaller echo area and shorter duration (Figs. 6a, d), always leading to less total precipitation (~2 × 10^4 mm; Fig. 6e). Their HPAR is often the highest in a day (up to 0.6), corresponding to the strongest convection cores and bringing the most intense precipitation. As CSs basically last for 1–3 h, intense precipitation usually appears in between 1400 and 1800 LT, and the most typical areal precipitation is 0.5–1 mm km^{-2}, accounting for more than 25.18% in this period (Fig. 7). The afternoon peak corresponds to the convective precipitation peak in Zheng et al. (2019) and can be explained by the fact that intense convection is often triggered by solar radiative heating at the land surface (Chen et al., 2018; Gao et al., 2019). In summary, CSs generated during 1400–1600 LT are characterized by the strongest convection and a smaller size, causing violent and transient showers but less total precipitation.

3.3 *Similar evolution between echo intensity and precipitation*

According to the strongest convection time and largest size time, the lifetimes of CSs are divided into rapid-de-

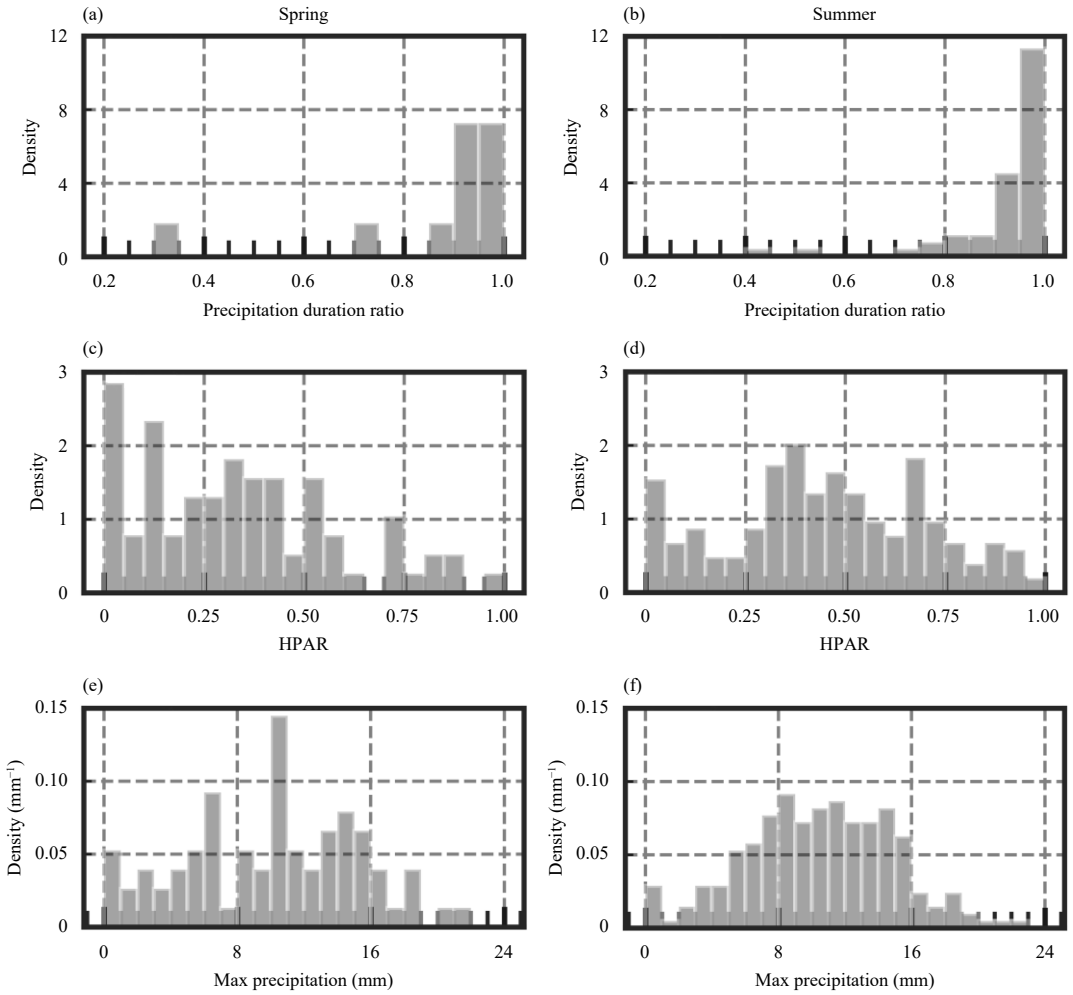

Fig. 4. Probability density histograms of (a, b) precipitation duration ratio, (c, d) maximum HPAR, and (e, f) maximum precipitation (mm) in 6 min in spring (left column) and summer (right column) CSs. The ordinate represents the probability density, which is the interval probability divided by the interval length. The horizontal axis represents values of precipitation characteristics.

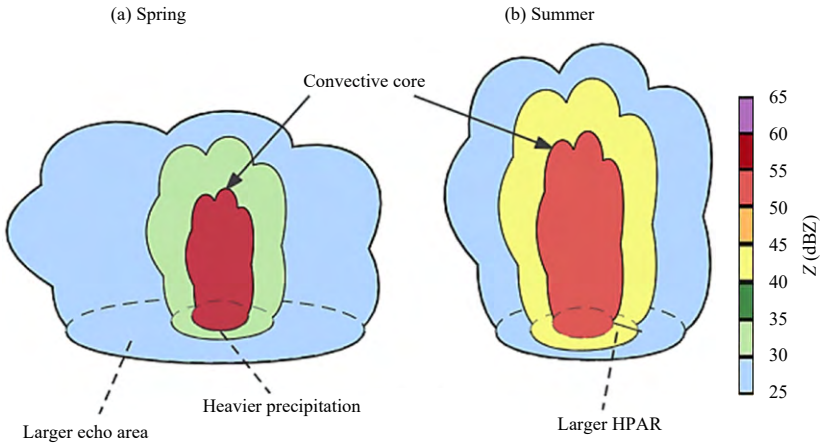

Fig. 5. Schematic of (a) spring and (b) summer CSs that produce short-term heavy precipitation in Hunan Province, central China.

veloping, mature, and dissipated stages (Fig. 8). In the rapid-developing stage (0–0.2), CSs expand quickly in size both horizontally and vertically with rapidly increasing echo intensity (Figs. 8a–c). In particular, the AER and convective fraction of CSs reach peaks at one-tenth of the normalized lifetime, which is ahead of the precipit-

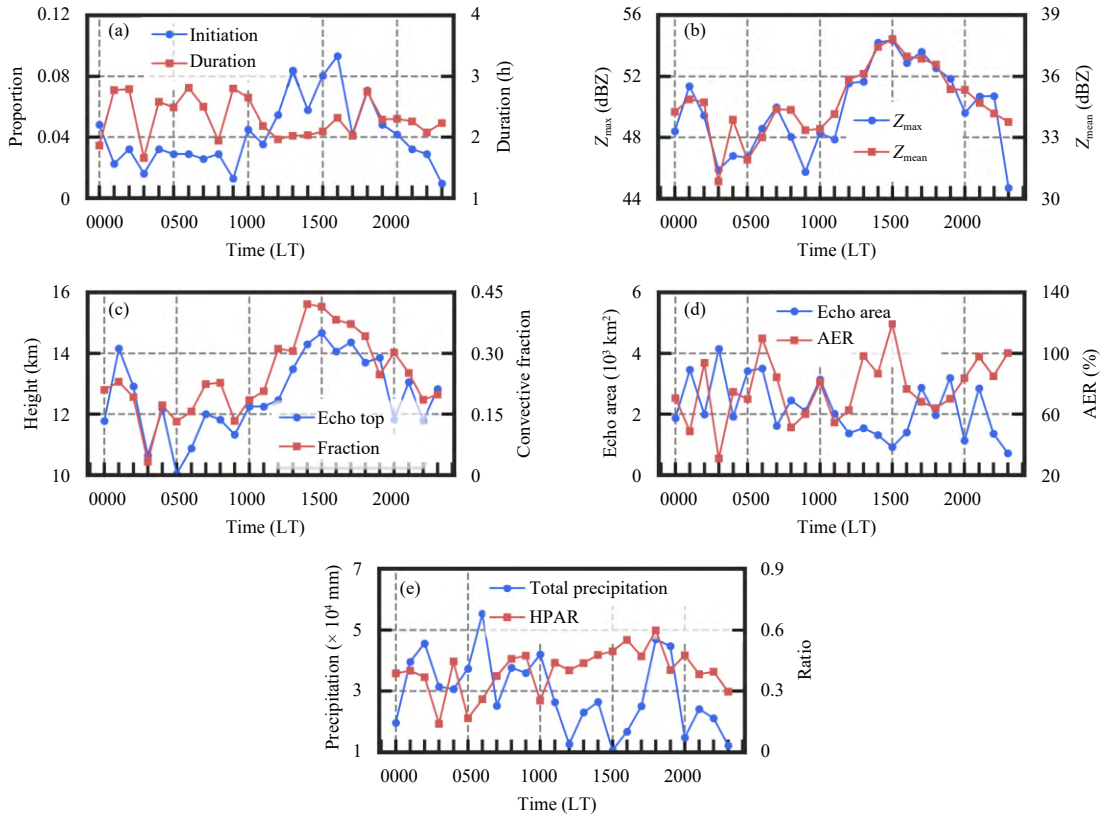

Fig. 6. (a) Frequency of CS initiation time (blue line) and duration at different times (red line; h), (b) Z_{max} (blue line; dBZ) and Z_{mean} (red line; dBZ) of CSs initiating at different times. (c–e) As in (b), but for (c) the maximum echo top (blue line; km) and convective fraction (red line), (d) the echo area (blue line; 10^3 km^2) and AER (red line; %), and (e) the total precipitation (blue line; 10^4 mm) and HPAR (red line).

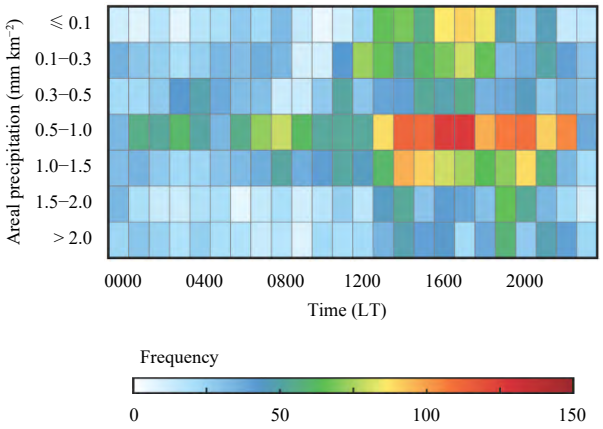

Fig. 7. Diurnal frequency distribution of areal precipitation (mm km^{-2}).

ation peak (Figs. 8a, b, d), which is important for early warnings of severe convective weather. In the mature stage (0.2–0.5), the echo top reaches a peak even though the mean intensity starts to weaken (Figs. 8b, c). After that, CSs gradually decline with shrinking echo area and negative AER in the dissipated stage (0.5–1). The evolution of Z_{mean} and areal precipitation are the most similar during the lifetime, emphasizing the important contribution of CS convective intensity to precipitation intensity (Figs. 8c, d).

4. Relationships among scale, intensity, and precipitation

According to the above analysis, surface precipitation is largely affected by the size and convective intensity of CSs. The spatial extent and convective intensity show significant linear correlations with the duration, increasing by 0.155 h per 10^3 km^2 and 0.0372 h per dBZ (Figs. 9a–c). This confirms that deeper convection develops as CSs maintain for longer (Moseley et al., 2013; Chen et al., 2020). However, a quadratic relation exists between the duration and AER (Fig. 9d). As the AER increases, the duration increases (decreases) when the AER is less than 50% (more than 50%); in other words, CSs with an AER value of 40%–50% tend to last longest. This relationship is not satisfied in the case of an AER over 70%. Similarly, the duration relates to the total precipitation in a quadratic function; moderate precipitation of (3–5) × 10^4 mm corresponds to the longest duration (3 h on average), except the group with extreme total precipitation

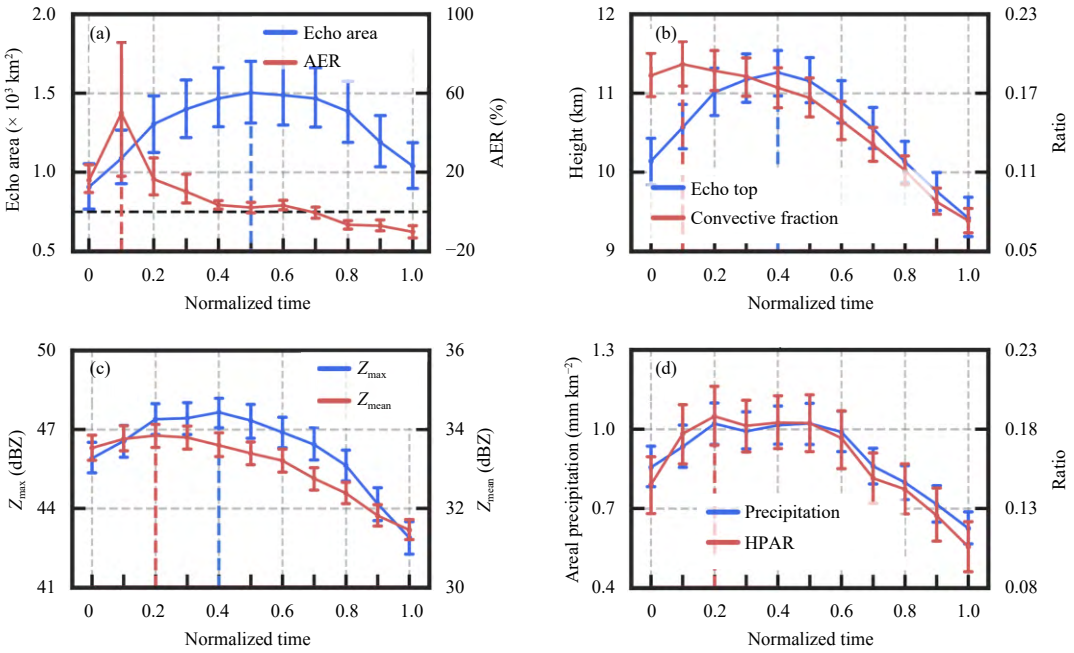

Fig. 8. Evolution of CS parameters during a standard CS lifetime: (a) echo area (blue line; 10^3 km^2) and AER (red line; %), in which the black dashed line indicates an AER of zero; (b) echo top (blue line; km) and convective fraction (red line); (c) Z_{max} (blue line; dBZ) and Z_{mean} (red line; dBZ); (d) areal precipitation (blue line; mm km^{-2}) and the HPAR (red line). The vertical solid line at each moment indicates the central 90% range of the parameter, and the vertical dashed line indicates the corresponding peak moment of parameters.

exceeding 9×10^4 mm (Fig. 9e).

Analogously, a remarkable linear relationship exists between the convective intensity and echo area (Figs. 10a, b). The AER and echo area show a slightly weak quadratic relationship (Fig. 10c). The fact that CSs with an AER of 40%–50% seem to maintain a wider echo area and longer duration (Figs. 9d, 10c) implies that CSs with a moderate AER easily produce more vigorous convection and thus maintain a larger spatiotemporal scale. A larger horizontal scale is the most critical factor for CSs to produce more precipitation, as its linear relationship with total precipitation has an R^2 as high as 0.982, increasing 10^4 mm of precipitation for every 71.1 km^2 (Fig. 10d). This quantitative relation could help with estimating the disaster-causing capacity of short-term heavy precipitation from the macroscopic size of CSs.

The convective intensity, echo area, and lifetime of CSs tend to be codependent on one another, and on the features that describe their evolution, like the AER (Kyznarová and Novák, 2009; Chen et al., 2021; Shehu and Haberlandt, 2022). Considering the above results, the spatiotemporal scale and precipitation of CSs are affected by the AER. In the case of total precipitation being less than 5×10^4 mm, CSs produce more precipitation with longer duration, which is a result of the increasing AER (Figs. 9d, e). In other words, CSs tend to maintain a longer duration, larger echo area, and produce more precipitation with the AER increasing when it is less than 50% (Figs. 9d, e, 10c). In the other case, CSs maintain for a shorter time while producing more total precipitation due to the larger AER (Figs. 9d, e, 10d). A large AER value (over 50%) means that the CS expands rapidly and results in increased precipitation because the echo area is the key contributor to the total precipitation. Meanwhile, the airflow is dominated by horizontal divergence when CSs expand rapidly, so the vertical updraft cannot be steadily maintained, restricting the development of convection and causing a shorter duration.

5. Summary and discussion

The macroscale characteristics of 595 CSs related to short-term heavy precipitation from April to September 2016–2018 in Hunan Province, central China, are analyzed in this paper using the IRT algorithm. The conclusions are as follows:

Summer CSs occur more frequently and develop more vigorously than spring CSs, and they usually last for a longer duration (2.4 h on average), have a higher echo top that can even reach 16 km, and produce stronger mean convection (35.6 dBZ on average). However, spring CSs cover larger horizontal ranges and contain stronger convective cores, corresponding to larger total precipitation of about 33,800 mm and heavier local precipitation. Such differences between spring and summer

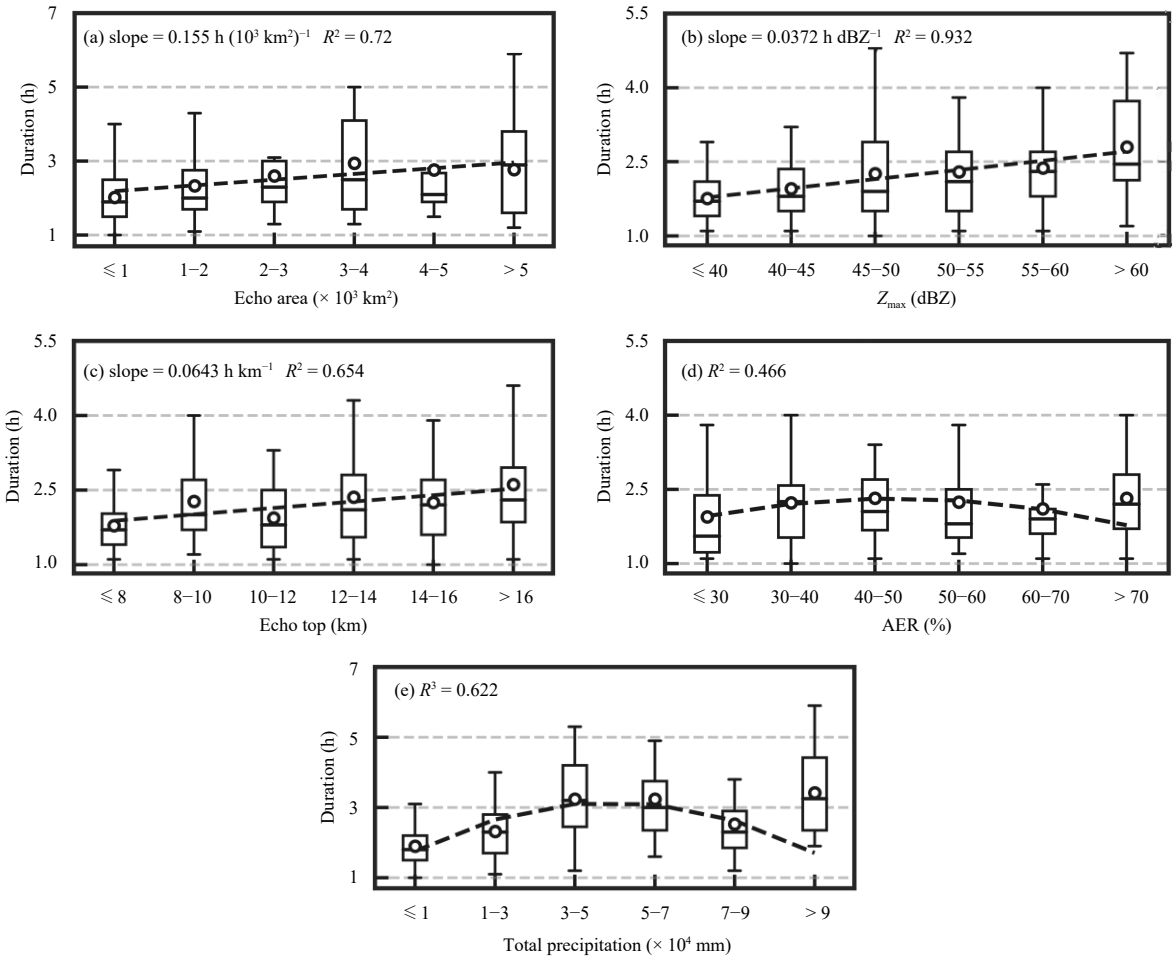

Fig. 9. As in Fig. 3, but boxplots showing the duration of CSs as a function of parameter groups: (a) maximum echo area (10^3 km^2), (b) Z_{max} (dBZ), (c) echo top (km), (d) maximum AER (%), and (e) total precipitation (10^4 mm). Horizontal coordinates represent CS groups with different parameter values. The black dashed lines in (a–c) are linear regressions for the average duration in each group, while in (d, e) they denote quadratic function fitting. The "slope" refers to the linear regression slope and R^2 represents the determination coefficient measuring the fitting goodness of the functions. All values of R^2 are significant at the 95% confidence level.

CSs also exist in the east of the US Rocky Mountains (Feng et al., 2019).

CSs initiate diurnally in a bimodal structure peaking at 1300 and 1600 LT, and thus the short-term heavy precipitation mostly happens in the afternoon. CSs occurring in the daytime tend to last for about 2 h, shorter than at night. CSs initiated during 1400–1600 LT are characterized by the strongest convection, causing violent and transient showers with typical areal precipitation reaching 0.5–1 mm km^{-2}. However, these CSs size are smaller and produce less total precipitation.

A linear correlation exists between the spatiotemporal scale and convective intensity of CSs, with the duration increasing by 0.155 h (0.0372 h) per 10^3 km^2 of area (dBZ of intensity). The echo area is found to be the most important parameter to precipitation, with a significant linear relation, increasing the precipitation by 10^4 mm for every 71.1 km^2. The relation between the duration and total precipitation depends on the AER. When the AER is less than 50%, CSs maintain a larger spatiotemporal scale and produce more precipitation as the AER increases. When the AER is over 50%, CSs maintain a shorter duration but expand rapidly and produce more precipitation as the AER increases.

Having analyzed the characteristics of CSs with short-term heavy precipitation in Hunan Province, this paper highlights that the CS initiation peak in this region is different to that of other regions, such as the Yangtze–Huai River basin (He et al., 2017) and South China (Li et al., 2021). Statistical results in Hunan Province indicate close relationships among the CS spatiotemporal scale, convective intensity, and related surface precipitation, which is consistent with previous research and thus provides a reference for CS characteristics in other regions (Moseley et al., 2013; Chen et al., 2020; Li et al., 2021, Shehu and Haberlandt, 2022). We have also ex-

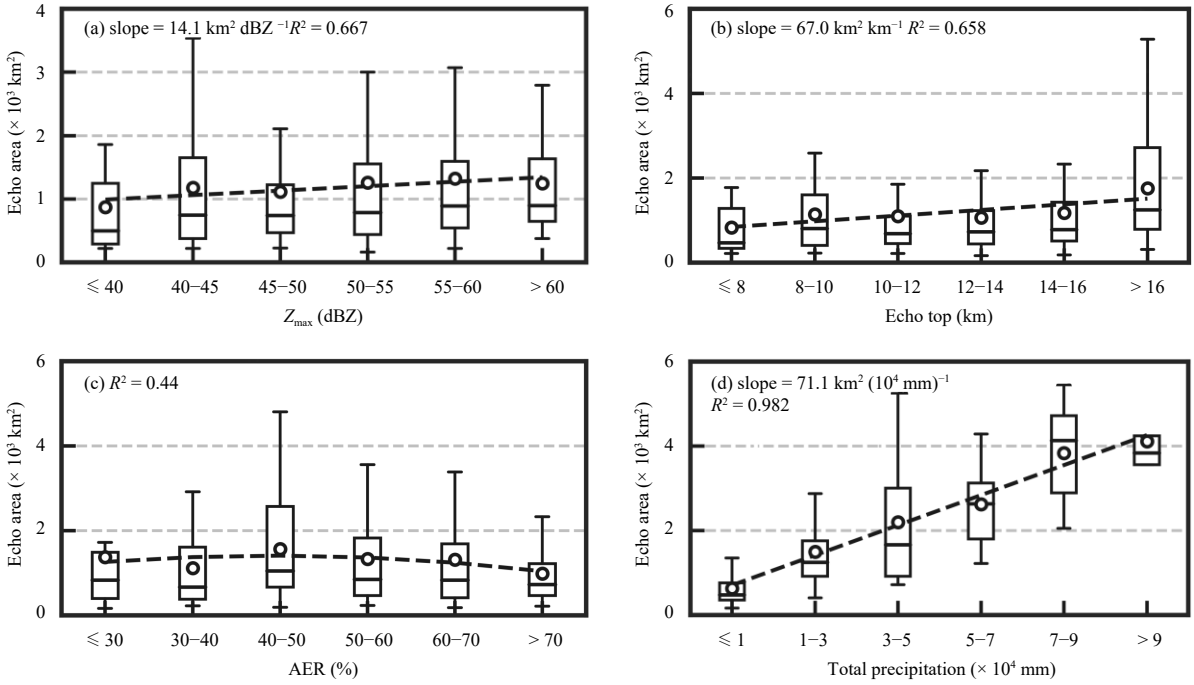

Fig. 10. As in Fig. 9, but for the maximum echo area: (a) Z_{max} (dBZ), (b) echo top (km), (c) maximum AER (%), and (d) total precipitation (10^4 mm). The black dashed lines in (a, b, d) show linear regressions of the average echo area, while in (c) it represents a quadratic fitting function.

plored these relationships quantitatively, which provides a reference for predicting the precipitation amount from the CSs characteristics. Further research is needed to explore the vertical structure and formation mechanism of CSs in Hunan Province, and even the whole of China, as well as the regional and topographic effects on the initiation and development of CSs.

Acknowledgments. We gratefully acknowledge the National Meteorological Information Centre, China Meteorological Administration for providing the dataset. We appreciate the valuable comments and suggestions from the anonymous reviewers.

REFERENCES

Berg, P., C. Moseley, and J. O. Haerter, 2013: Strong increase in convective precipitation in response to higher temperatures. *Nat. Geosci.*, **6**, 181–185, doi: 10.1038/ngeo1731.

Carvalho, L. M. V., and C. Jones, 2001: A satellite method to identify structural properties of mesoscale convective systems based on the maximum spatial correlation tracking technique (MASCOTTE). *J. Appl. Meteor.*, **40**, 1683–1701, doi: 10.1175/1520-0450(2001)040<1683:ASMTIS>2.0.CO;2.

Chen, D. D., J. P. Guo, H. Q. Wang, et al., 2018: The cloud top distribution and diurnal variation of clouds over east Asia: Preliminary results from advanced Himawari imager. *J. Geophys. Res. Atmos.*, **123**, 3724–3739, doi: 10.1002/2017JD028044.

Chen, D. D., J. P. Guo, D. Yao, et al., 2019: Mesoscale convective systems in the Asian monsoon region from advanced Himawari imager: Algorithms and preliminary results. *J. Geophys. Res. Atmos.*, **124**, 2210–2234, doi: 10.1029/2018JD029707.

Chen, D. D., J. P. Guo, D. Yao, et al., 2020: Elucidating the life cycle of warm-season mesoscale convective systems in eastern China from the Himawari-8 geostationary satellite. *Remote Sens.*, **12**, 2307, doi: 10.3390/rs12142307.

Chen, M. X., Y. C. Wang, F. Gao, et al., 2012: Diurnal variations in convective storm activity over contiguous North China during the warm season based on radar mosaic climatology. *J. Geophys. Res. Atmos.*, **117**, D20115, doi: 10.1029/2012JD018158.

Chen, Y. L., A. Q. Zhang, Y. F. Fu, et al., 2021: Morphological characteristics of precipitation areas over the Tibetan Plateau measured by TRMM PR. *Adv. Atmos. Sci.*, **38**, 677–689, doi: 10.1007/s00376-020-0233-1.

Cristiano, E., M.-C. ten Veldhuis, and N. van de Giesen, 2017: Spatial and temporal variability of rainfall and their effects on hydrological response in urban areas–a review. *Hydrol. Earth Syst. Sci.*, **21**, 3859–3878, doi: 10.5194/hess-21-3859-2017.

Feng, Z., R. A. Jr. Houze, L. R. Leung, et al., 2019: Spatiotemporal characteristics and large-scale environments of mesoscale convective systems east of the Rocky Mountains. *J. Climate*, **32**, 7303–7328, doi: 10.1175/JCLI-D-19-0137.1.

Fu, Y. F., Y. L. Chen, X. D. Zhang, et al., 2020: Fundamental characteristics of tropical rain cell structures as measured by TRMM PR. *J. Meteor. Res.*, **34**, 1129–1150, doi: 10.1007/s13351-020-0035-5.

Futyan, J. M., and A. D. del Genio, 2007: Deep convective system evolution over Africa and the tropical Atlantic. *J. Climate*, **20**, 5041–5060, doi: 10.1175/JCLI4297.1.

Gao, C. C., Y. Y. Li, and H. W. Chen, 2019: Diurnal variations of

different cloud types and the relationship between the diurnal variations of clouds and precipitation in central and East China. *Atmosphere*, **10**, 304, doi: 10.3390/atmos10060304.

Goudenhoofdt, E., and L. Delobbe, 2013: Statistical characteristics of convective storms in Belgium derived from volumetric weather radar observations. *J. Appl. Meteor. Climatol.*, **52**, 918–934, doi: 10.1175/JAMC-D-12-079.1.

Haberlie, A. M., and W. S. Ashley, 2018: A method for identifying midlatitude mesoscale convective systems in radar mosaics. Part II: Tracking. *J. Appl. Meteor. Climatol.*, **57**, 1599–1621, doi: 10.1175/JAMC-D-17-0294.1.

He, Z. W., Q. H. Zhang, L. Q. Bai, et al., 2017: Characteristics of mesoscale convective systems in central East China and their reliance on atmospheric circulation patterns. *Int. J. Climatol.*, **37**, 3276–3290, doi: 10.1002/joc.4917.

Hou, J. Y., and P. Wang, 2017: Storm tracking via tree structure representation of radar data. *J. Atmos. Oceanic Technol.*, **34**, 729–747, doi: 10.1175/JTECH-D-15-0119.1.

Houze, R. A. Jr., 2018: 100 years of research on mesoscale convective systems. *Meteor. Monogr.*, **59**, 17.1–17.54, doi: 10.1175/AMSMONOGRAPHS-D-18-0001.1.

Houze, R. A. Jr., K. L. Rasmussen, M. D. Zuluaga, et al., 2015: The variable nature of convection in the tropics and subtropics: A legacy of 16 years of the tropical rainfall measuring mission satellite. *Rev. Geophys.*, **53**, 994–1021, doi: 10.1002/2015RG000488.

Hu, L., D. F. Deng, S. T. Gao, et al., 2016: The seasonal variation of Tibetan convective systems: Satellite observation. *J. Geophys. Res. Atmos.*, **121**, 5512–5525, doi: 10.1002/2015JD024390.

Kyznarová, H., and P. Novák, 2009: CELLTRACK—convective cell tracking algorithm and its use for deriving life cycle characteristics. *Atmos. Res.*, **93**, 317–327, doi: 10.1016/j.atmosres.2008.09.019.

Lakshmanan, V., and T. Smith, 2010: An objective method of evaluating and devising storm-tracking algorithms. *Wea. Forecasting*, **25**, 701–709, doi: 10.1175/2009WAF2222330.1.

Lan, M. C., F. Huo, L. Zhou, et al., 2022: Mechanisms of short-duration heavy rainfall in the western Pacific subtropical high area: An analysis of two rainstorms of 2018 in Hunan Province, China. *Atmosphere–Ocean*, **60**, 1–12, doi: 10.1080/07055900.2022.2060177.

Lavanya, S., N. V. P. Kirankumar, S. Aneesh, et al., 2019: Seasonal variation of raindrop size distribution over a coastal station Thumba: A quantitative analysis. *Atmos. Res.*, **229**, 86–99, doi: 10.1016/j.atmosres.2019.06.004.

Li, S., Z. Y. Meng, and N. G. Wu, 2021: A preliminary study on the organizational modes of mesoscale convective systems associated with warm-sector heavy rainfall in South China. *J. Geophys. Res. Atmos.*, **126**, e2021JD034587, doi: 10.1029/2021JD034587.

Liu, Y., D.-G. Xi, Z.-L. Li, et al., 2014: Automatic tracking and characterization of cumulonimbus clouds from FY-2C geostationary meteorological satellite images. *Adv. Meteor.*, **2014**, 478419, doi: 10.1155/2014/478419.

Ma, R. Y., J. H. Sun, and X. L. Yang, 2021: A 7-yr climatology of the initiation, decay, and morphology of severe convective storms during the warm season over North China. *Mon. Wea. Rev.*, **149**, 2599–2612, doi: 10.1175/MWR-D-20-0087.1.

Mai, Z., S. M. Fu, J. H. Sun, et al., 2021: Key statistical characteristics of the mesoscale convective systems generated over the Tibetan Plateau and their relationship to precipitation and southwest vortices. *Int. J. Climatol.*, **41**, E875–E896, doi: 10.1002/joc.6735.

Marra, F., E. I. Nikolopoulos, J. D. Creutin, et al., 2016: Space-time organization of debris flows-triggering rainfall and its effect on the identification of the rainfall threshold relationship. *J. Hydrol.*, **541**, 246–255, doi: 10.1016/j.jhydrol.2015.10.010.

Meng, Z. Y., D. C. Yan, and Y. J. Zhang, 2013: General features of squall lines in East China. *Mon. Wea. Rev.*, **141**, 1629–1647, doi: 10.1175/MWR-D-12-00208.1.

Meredith, E. P., U. Ulbrich, and H. W. Rust, 2023: Cell tracking of convective rainfall: Sensitivity of climate-change signal to tracking algorithm and cell definition (cell-TAO v1.0). *Geosci. Model Dev.*, **16**, 851–867, doi: 10.5194/gmd-16-851-2023.

Moseley, C., P. Berg, and J. O. Haerter, 2013: Probing the precipitation life cycle by iterative rain cell tracking. *J. Geophys. Res. Atmos.*, **118**, 13,361–13,370, doi: 10.1002/2013JD020868.

Moseley, C., O. Henneberg, and J. O. Haerter, 2019: A statistical model for isolated convective precipitation events. *J. Adv. Model. Earth Syst.*, **11**, 360–375, doi: 10.1029/2018MS001383.

Nissen, S. B., and J. O. Haerter, 2021: Circling in on convective self-aggregation. *J. Geophys. Res. Atmos.*, **126**, e2021JD035331, doi: 10.1029/2021JD035331.

Peter, J. R., M. J. Manton, R. J. Potts, et al., 2015: Radar-derived statistics of convective storms in Southeast Queensland. *J. Appl. Meteor. Climatol.*, **54**, 1985–2008, doi: 10.1175/JAMC-D-13-0347.1.

Rasmussen, K. L., M. M. Chaplin, M. D. Zuluaga, et al., 2016: Contribution of extreme convective storms to rainfall in South America. *J. Hydrometeor.*, **17**, 353–367, doi: 10.1175/JHM-D-15-0067.1.

Samanta, S., P. Murugavel, D. Gurnule, et al., 2021: The life cycle of a stationary cloud cluster during the Indian summer monsoon: A microphysical investigation using polarimetric C-band radar. *Mon. Wea. Rev.*, **149**, 3761–3780, doi: 10.1175/MWR-D-20-0274.1.

Schroeer, K., G. Kirchengast, and O. Sungmin, 2018: Strong dependence of extreme convective precipitation intensities on gauge network density. *Geophys. Res. Lett.*, **45**, 8253–8263, doi: 10.1029/2018GL077994.

Shehu, B., and U. Haberlandt, 2022: Improving radar-based rainfall nowcasting by a nearest-neighbour approach—Part 1: Storm characteristics. *Hydrol. Earth Syst. Sci.*, **26**, 1631–1658, doi: 10.5194/hess-26-1631-2022.

Sun, G. R., Y. Y. Li, and S. C. Li, 2019: The differences in cloud vertical structures between active and break spells of the East Asian summer monsoon based on CloudSat data. *Atmos. Res.*, **224**, 157–167, doi: 10.1016/j.atmosres.2019.03.035.

Tian, F. Y., Y. G. Zheng, T. Zhang, et al., 2015: Statistical characteristics of environmental parameters for warm season short-duration heavy rainfall over central and eastern China. *J. Meteor. Res.*, **29**, 370–384, doi: 10.1007/s13351-014-4119-y.

Utsav, B., S. M. Deshpande, S. K. Das, et al., 2017: Statistical characteristics of convective clouds over the western Ghats

derived from weather radar observations. *J. Geophys. Res. Atmos.*, **122**, 10,050–10,076, doi: 10.1002/2016JD026183.

Xiong, A. Y., N. Liu, Y. J. Liu, et al., 2022: QpefBD: A benchmark dataset applied to machine learning for minute-scale quantitative precipitation estimation and forecasting. *J. Meteor. Res.*, **36**, 93–106, doi: 10.1007/s13351-022-1140-4.

Yao, R., J. Tang, X. L. Wang, et al., 2020: Temporal-spatial distribution of short-time heavy rainfall in Hunan and statistical analysis of related environmental parameters. *J. Catastrophol.*, **35**, 116–121, doi: 10.3969/j.issn.1000-811X.2020.02.022. (in Chinese)

Zhang, A. Q., C. Chen, Y. L. Chen, et al., 2022: Resilient dataset of rain clusters with life cycle evolution during April to June 2016–2020 over eastern Asia based on observations from the GPM DPR and Himawari-8 AHI. *Earth Syst. Sci. Data*, **14**, 1433–1445, doi: 10.5194/essd-14-1433-2022.

Zhang, X. D., W. Q. Shen, X. Y. Zhuge, et al., 2021: Statistical characteristics of mesoscale convective systems initiated over the Tibetan Plateau in summer by Fengyun satellite and precipitation estimates. *Remote Sens.*, **13**, 1652, doi: 10.3390/rs13091652.

Zheng, L. L., J. H. Sun, X. L. Zhang, et al., 2013: Organizational modes of mesoscale convective systems over central East China. *Wea. Forecasting*, **28**, 1081–1098, doi: 10.1175/WAF-D-12-00088.1.

Zheng, Y. G., Y. D. Gong, J. Chen, et al., 2019: Warm-season diurnal variations of total, stratiform, convective, and extreme hourly precipitation over central and eastern China. *Adv. Atmos. Sci.*, **36**, 143–159, doi: 10.1007/s00376-018-7307-3.

Tech & Copy Editor: Zhirong CHEN